Usher, P., Kendall, J. M., Kelly, C. M., & Rietbrock, A. (2017). Measuring changes in fracture properties from temporal variations in anisotropic attenuation of microseismic waveforms. *Geophysical Prospecting*, *65*(S1), 347-362. https://doi.org/10.1111/1365-2478.12551

Measuring changes in fracture properties from temporal variations in anisotropic attenuation of microseismic waveforms

P. J. Usher*†§, J-M. Kendall†, C. M. Kelly‡, A. Rietbrock‡

* *Corresponding Author: philip.usher.2011@my.bristol.ac.uk*

† *University of Bristol, Earth Sciences, Bristol, UK*

‡ *University of Liverpool, School of Environmental Sciences, Geology and Geophysics*

Liverpool, UK

§ *Now at Itasca IMaGE,*

Shrewsbury, UK

(June 11, 2017)

Running head: **Changes in fracture properties from microseismic attenuation**

ABSTRACT

We investigate fracture induced attenuation anisotropy in a cluster of events from a microseismic dataset acquired during hydraulic fracture stimulation. The dataset contains 888 events of magnitude -3.0 to 0.0. We use a log-spectral-amplitude-ratio method to estimate change in t^* over a half hour time period where fluid is being injected and an increase in fracturing from S-wave splitting analysis has been previously inferred. A Pearson's correlation analysis is used to assess whether or not changes in attenuation with time are statistically significant. P-waves show no systematic change in t^* during this time. In contrast, S-waves polarised perpendicular to the fractures show a clear and statistically significant increase with time, whilst S-waves polarised parallel to the fractures show a weak negative trend.

We also compare t^* between the two S-waves, finding an increase in Δt^* with time. A poroelastic rock physics model of fracture-induced attenuation anisotropy is used to interpret the results. This model suggests that the observed changes in t* are related to an increase in fracture density of up to 0.04. This is much higher than previous estimates of 0.025 ± 0.002 based on S-wave velocity anisotropy, but there is considerably more scatter in the attenuation measurements. This could be due to the added sensitivity of attenuation measurement to non-aligned fractures, fracture shape, and fluid properties. Nevertheless, this pilot study shows that attenuation measurements are sensitive to fracture properties such as fracture density and aspect ratio.

INTRODUCTION

Fractures provide important pathways for fluid flow, especially in porous rocks with low matrix permeability (e.g. carbonates, (Al-Harrasi 2010)). Fractures can be naturally occurring or may be induced through hydraulic fracture stimulation. Understanding fractures and fracturing is important in many reservoir systems, including those associated with petroleum exploitation, geothermal energy production and magma migration. It has been long known that fluids in fractured and porous rock will cause significant attenuation in seismic energy propagation (Toksöz et al. 1979). Furthermore, fractures have a tendency to align in fracture sets, which leads to directional dependencies in seismic wave propagation, or seismic anisotropy. Here we consider attenuation anisotropy in fractured fluid-filled rock in a petroleum setting, showing how this can provide a means for monitoring fracture network development and fluid infiltration.

A major indicator of fracture-induced anisotropy is S-wave splitting. An initially polarised S-wave will split into orthogonally polarised fast and slow S-waves when entering a region of aligned fractures. The fracture spacing must be on a smaller length scale than the dominant seismic wavelength. The degree of separation between the two S-waves is proportional to the fracture density and the spatial extent of the fracturing. The polarisation of the S-waves is an indicator of the fracture orientation. S-wave splitting in fractured systems has been observed in a number of environments including volcanic and petroleum settings (Johnson et al. (2011), Teanby et al. (2004)).

In the petroleum setting considered in this paper, we have multiple sources of anisotropy from a combination of fractures and bedding but the ray geometries we deal with are mostly sensitive to the fractures. We therefore measure attenuation from the components of S-wave

polarised perpendicular, $S_{\perp}$, and parallel, $S_{\parallel}$, to the fractures.

Changes in attenuation in fluid-filled fractured systems has been observed in a number of settings. Titzschkau et al. (2010) look at variations in attenuation from coda waves and P-waves at Mt. Ruapehu Volcano, New Zealand. They propose that the attenuation observations are linked to velocity anisotropy observations and propose that this is due to stress changes caused by magma dykes. Kelly et al. (2013) observed temporal variations in P-wave attenuation before and after the 2004 M6.0 Parkfield earthquake. They attributed this variation to fracture dilatancy due to changes in stress conditions and fluid pressure before and after the earthquake.

Aligned fracture sets lead to directional variations in both velocity and attenuation (Chapman 2003). There have been only a few documented field observations of this effect. The log-spectral-amplitude-ratio method was applied to vertical seismic profiles (Maultzsch et al. 2007). Variations in attenuation with offset (Dasgupta and Clark 1998) and azimuth (Shen et al. 2002; Clark et al. 2001; Chichinina et al. 2006) have been examined in seismic reflection surveys. Chapman (2003) presented a numerical model of how frequency-dependent S-wave splitting is sensitive to dominant fracture size. Al-Harrasi et al. (2011) have used such observations in microseismic data from an oilfield to infer significant changes in fracture dimensions between a carbonate reservoir and the overlying shale cap-rock.

Passive seismic monitoring in petroleum settings is a rapidly developing area of research, primarily spurred on by the need to monitor hydraulic fracture stimulation in shale gas reservoirs (Maxwell 2010). "Clouds" of induced microseismic events are used as a proxy for the extent of fracture stimulation, often referred to as the stimulated reservoir volume. S-wave splitting measurements can be used to further characterise the style of induced

fractures, including their compliances (Wuestefeld et al. 2011; Baird et al. 2013b; Verdon and Wüstefeld 2013). Here we go a step further and study temporal variations in S-wave attenuation in microseismic events recorded during a period of fluid injection into a tight-gas sandstone. We consider changes in both the fast $S_{\parallel}$ and slow $S_{\perp}$ phases using log-spectral-amplitude-ratios based on a reference event in the sequence. We also consider log-spectral-amplitude-ratios between the fast $S_{\parallel}$ and slow $S_{\perp}$ phases for each event. This follows the approaches of Carter and Kendall (2006) and Kelly et al. (2013).

We start by introducing the dataset used in the study, then outline the theoretical framework and modelling carried out using the approach of Chapman (2003) for attenuation anisotropy. This is followed by a description of the methodology for estimating attenuation anisotropy using log-spectral-amplitude-ratios. The resulting measurements are then interpreted by means of an inversion for fracture properties.

DATASET

Fluid was injected into the tight sandstones of the Carthage Cotton Valley gas field in East Texas, as part of an experiment funded by a consortium of oil field operators, service companies, U.S. government agencies and national laboratories in the mid 1990's (Walker 1997). Part of the experiment, treatment B, targeted the very fine-grained thin interbedded shales and sands (Walker 1997) of the Rosebury, Ardis, Justiss and "E" sand members which lie at a depth of 2575–2838 m (Rutledge et al. 2004).

The seismicity was measured by two arrays of borehole geophones with a sampling rate of 1000 Hz (Walker 1997). The recorded frequencies are between 30–500 Hz, although the top end of this frequency range could be affected by anti-aliasing filters. The geophone

spacing is not constant and varies from 14–260 m. The first array consists of four geophones 550 m above the formation of interest and located 320 m east of the injection well. The second array has 16 geophones and extends 450 m above the target unit. It is located 390 m northeast of the injection well (Figure 1).

Rutledge et al. (2004) located 888 events using a three layer velocity model. Most of these events cluster along a strike of 80°, except for a spur of events containing 42 % of the measurements which has an orientation of 65° (Figure 1, inset). Rutledge et al. (2004) also calculated source mechanisms for the events and found them to be mostly strike slip. The events from the spur show fault planes trending 65°, however other events north-east of the injection well show fault planes trending 85°.

Wuestefeld et al. (2011) interpreted S-wave splitting measurements as anisotropy due to the bedding and an aligned fracture set orientated at 60°, oblique to the trend of the fracture corridor (83°). A cluster of events between 9:20 and 10:00 show particularly clear temporal variations in the S-wave splitting measurements (Figure 2a). This time period corresponded to the third period of injection (Figure 2b). They inverted for fracture properties using the method of Verdon et al. (2009) and found that the fracture density (the number of fractures per unit volume) increased from 0.025–0.035 but there was no change in fracture strike (Figure 2c and Figure 2d).

In this paper we use this cluster of 42 events and a receiver located in the middle of the first array. This selection showed the clearest increase in shear-wave splitting and thus has strong sensitivity to the fracture network. In our modelling we examine the effects of fractures within an isotropic velocity. We are dealing with a narrow range of ray paths which are travelling at angles much less than 45° to the vertical. In this direction, the effects

of fractures on the orthorhombic anisotropy are much stronger than the effects of the VTI anisotropy due to the intrinsic rock fabric (see Figure 5 in Wuestefeld et al. (2011) and Figure 6 in Verdon and Wüstefeld (2013)). We can therefore treat the changes in velocity due to a VTI anisotropy as being negligible and the isotopic velocities as being representative of the velocities at our ray path azimuths and inclinations. However, in order to use the full range of ray paths from the experiment, we would need to fully account for both the VTI and fracture-induced anisotropy that contribute to the overall orthorhombic symmetry. We do use the orthorhombic anisotropy from Wuestefeld et al. (2011) to find our two S-wave components in the data analysis.

SQUIRT FLOW MODEL

There are numerous mechanisms for seismic attenuation including more intrinsic effects associated with absorption from frictional heat loss. However, it is appealing to measure more extrinsic mechanisms such as those associated with poroelasticity and scattering, as these will be very sensitive to properties such as fluid content and fracture/pore size (e.g., Baird et al. (2013a)). To understand the causative mechanisms is difficult and we normally refer to an 'effective' attenuation. Toksöz and Johnston (1981) rule out some of the simpler mechanisms of attenuation such as frictional grain sliding and bulk fluid flow for the field scale but suggest that a squirt flow mechanism would be observable at the field scale. Baird et al. (2013a) came to a similar conclusion considering the microseismic response of frequency dependent anisotropy in fractured media. We therefore focus on attenuation due to squirt flow in fractured porous rock.

We model frequency dependent anisotropy due to squirt flow in porous fractured media using the theory of Chapman (2003). Seismic waves propagating through fractured porous

rocks can induce pressure gradients that cause fluid exchange between fractures and pore spaces to achieve pressure equalisation (e.g., Chapman (2003)). At low frequencies the fluid drains slowly from the fractures and does not cause significant energy loss. At high frequencies the fluid does not have time to leave the fractures and so is trapped there making the fractures stiff and only increasing the overall seismic velocity. However there is a characteristic frequency at which attenuation is maximum. This is calculated using the method of Chapman et al. (2003), which relates the characteristic frequency to grain size, fracture radius, permeability and viscosity. This model has been previously used to describe attenuation anisotropy observed in multi-azimuth VSP data from the Clair field in UK waters west of the Shetland Islands (Maultzsch et al. 2007). It has also been used to interpret frequency dependent S-wave splitting in microseismic data from an Omani oilfield in terms of fracture size (Al-Harrasi et al. 2011).

The Chapman (2003) model is a poroelastic equivalent medium model that considers the effects of randomly oriented microcracks and spherical pores with superimposed aligned sets of fractures. It is sensitive to matrix properties, including intrinsic anisotropy due to crystal-preferred-orientation, fluid properties, and fracture properties such as size, aspect ratio and fracture density. Another very important consideration is the direction of ray propagation for example, rays travelling parallel to fractures will be affected very differently from those cross-cutting the fractures.

MODELLING ATTENUATION AT COTTON VALLEY

To use the model of Chapman (2003), we estimated the ray, rock, fluid and fracture properties from the literature and the data. We calculate the variations in attenuation from a default model using a single value for each parameter. We then vary each parameter within

their ranges (Table 1). The attenuation is expressed as t^*, which is defined as:

$$t^* = \int_{path} \frac{1}{VQ} ds, \tag{1}$$

where Q is the quality factor, and V is the velocity. This means that t^* is the travel time modified by attenuation. Q is defined, under certain conditions, as the loss of amplitude per wavelength,

$$\frac{1}{Q} = -\frac{1}{\pi} \frac{\Delta A}{A}, \tag{2}$$

where A is the maximum particle velocity or a stress component and ΔA is amplitude lost in each cycle (Aki and Richards 2002).

As the medium is anisotropic, two independent S-waves will propagate each experiencing different amounts of attenuation. We assume a single set of vertical fractures which leads to two split S-waves polarised perpendicular, $S_\perp$, and parallel, $S_\parallel$ to the fractures.

A readily apparent effect in the results is that the fast $S_\parallel$ phase (Figure 3) does not experience any attenuation due to fractures, as this wave is polarised parallel to the plane of the fractures. The maximum amount of attenuation is seen in the slow $S_\perp$ phase and the P-wave shows intermediate amounts of attenuation.

The properties of the ray (e.g., frequency content, path length, direction) affect how much attenuation is experienced. Figure 3 shows that longer ray paths and frequencies close to the characteristic frequency show the most attenuation. Attenuation of the $S_\perp$ phase is maximum when the ray is travelling parallel to the plane of the fractures.

There are few reported values for porosity, permeability, bulk modulus and viscosity of the Cotton Valley rocks and fluids available, and they often have large variability. Thus we explore how rock and fluid parameters, which sometimes vary over orders of magnitude,

affect t^* (Figure 4). Attenuation varies in a non-linear way as a function of the bulk modulus and viscosity of the fluid, and porosity and permeability of the rock. Rock and fluid properties cause variations in t^* of $<0.003\,\mathrm{s}$.

Figure 5 shows the effects of different fracture properties on attenuation. The attenuation diminishes quickly as fracture aspect ratio approaches one (i.e., the fractures become more spherical), but a more complicated dependence on fracture radius is evident. The attenuation of the $S_\perp$ phase is greatest in directions parallel to the fractures (90° in this case), the P-wave shows intermediate variation and the $S_\parallel$ phase does not vary with fracture strike. S-wave splitting delay time is also at a maximum when the ray is propagating parallel to the fractures.

Another conclusion that can be drawn from Figure 5 is that the fracture-related attenuation is most sensitive to fracture density. A fracture density of 0.10 produces relatively large amounts of attenuation (t^* of up to $0.12\,\mathrm{s}$) compared to that due to other fracture, fluid or rock properties (t^* of $<0.03\,\mathrm{s}$). Only very small aspect ratios (<0.001) produce comparable amounts of attenuation.

Many approaches to measuring attenuation assume frequency independent attenuation (e.g., log-spectral-amplitude-ratio methods (Kelly et al. 2013)). However, fracture-induced anisotropy is frequency dependent, an attribute that can be used to estimate fracture size (e.g., Maultzsch et al. (2007); Al-Harrasi et al. (2011)). From our modelling, t^* is dependent on frequency (Figure 6) for a range of fracture densities. The effect is more acute for larger fracture densities. In this paper we use the log-spectral-amplitude-ratio method to estimate t^*, so we seek a frequency range where the attenuation effects are constant. The work of Wuestefeld et al. (2011) has estimated fracture densities of less than 0.04 for the Cotton

Valley dataset. We therefore restrict ourselves to the frequency range 200–400 Hz, where there is little variation in t^* (Figure 6). This assumption quickly breaks down for larger fracture densities. In the next section we describe our approach for estimating t^* in fracture-induced anisotropic media.

LOG-SPECTRAL-AMPLITUDE-RATIO METHOD

One of the most common approaches to measuring attenuation is the log-spectral-amplitude-ratio method (Båth 1974), and here we adopt the approach of Kelly et al. (2013). The technique is attractive in its simplicity, but has the drawback that it implicitly assumes frequency-independent Q. It provides a measure of differential attenuation between a signal and a reference signal, and thereby quantifies the difference in energy loss per cycle experienced by each signal. Here we adopt two approaches: one compares every event in our cluster (Figure 2) with some reference event in the cluster; the other approach follows the method of Carter and Kendall (2006) and compares the two split S-waves to each other.

The log-spectral-amplitude-ratio approach yields an estimate of Δt^*, as described below. The amplitude spectrum measured at a receiver can be described as,

$$A(f) = A(f)_s G \exp\left(-\pi f t^*\right), \tag{3}$$

where $A(f)$ is the amplitude spectra, $A(f)_s$ is the source amplitude, G includes any effects of propagation such as geometric spreading or receiver response, and f is frequency. The logarithm of the ratio of amplitudes for two signals (e.g., two earthquakes in the cluster shown in Figure 2) can be written as,

$$ln(\frac{A_1}{A_2}) = ln\frac{A_{s1}G_{s1}}{A_{s2}G_{s2}} + \pi f \Delta t^*. \tag{4}$$

A plot of the log-spectral-amplitude-ratio ($ln(\frac{A_1}{A_2})$) versus frequency (f) will produce a straight line with a gradient proportional to Δt^*. The term Δt^* can be thought of as the difference in attenuation integrated over the traveltime along the raypath for each event. We endeavour to use events that are co-located in order to avoid using a correction for differences in the raypaths between the two signals - that is to say $G_{s1} = G_{s2}$. Figure 7 illustrates the procedure for estimating the gradient to find Δt^*.

To obtain amplitude spectra, we initially define a 50 ms window around the signal and the reference signal. The three-component seismograms are then rotated into a ray centred coordinate system, where the radial component should primarily contain the P-wave, and the orthogonal components contain the $S_{\parallel}$ and $S_{\perp}$ phases, as estimated from S-wave splitting analysis. This is done by assuming a straight ray from the event location to the receiver.

A fast-Fourier-transform is taken of the pre-event noise and the event. We omit any points within the spectra where the signal is smaller than the noise. The log-spectral-amplitude-ratio of the signal relative to the reference is then plotted as a function of frequency. A robust weighted bisquare linear least-squares fitting method, with weights corresponding to the signal to noise ratio (SNR), is used to estimate the gradient, which is divided by π to yield Δt^*. The 95 % confidence limit is used as an error in Δt^*. As motivated in the previous section, we only consider the signal in the region of 200–400 Hz, a range over which Q can be assumed to be constant.

The sensitivity of the method to corner frequency cut-off and SNR is tested using synthetic spectra (Figure 8). To create the synthetic spectra we use,

$$\begin{aligned} \Omega_D(f) &= C_0 M_0 & f < f_C, \\ \Omega_D(f) &= C_0 M_0 \frac{1}{(f^2/f_C^2)} & f \geq f_C, \end{aligned} \tag{5}$$

where $\Omega_D(f)$ is the spectra as a function of frequency, C_0 is a constant dependent on the radiation pattern, M_0 is the seismic moment and, f_C is the corner frequency (Eisner et al. (2013) ; Aki and Richards (2002)). We then attenuate these source spectra using equation 3, and a Q of 100 for the reference event and a Q of 40 for the other. Gaussian noise is added to create different spectra with different SNR and a range of corner frequencies is used from 50–500 Hz. M_0 cancels out in the log-spectral-amplitude-ratio.

Figure 8a shows synthetic log-spectral-amplitude-ratios for events with corner frequencies from 50–500 Hz and a reference event with a corner frequency of 300 Hz. Amplitude spectra are theoretically flat below the corner frequency. For this reason and as shown in Figure 8a we need to measure the gradient of the log-spectral-amplitude-ratio below the corner frequency of both events. The corner frequency is dependent on magnitude, therefore we need events with corner frequencies above 400 Hz - the top end of the frequency range selected.

Figure 8b shows log-spectral-amplitude-ratios for events with signal to noise ratios (SNR) from 1–5, with a reference event with a SNR of 5. We used a corner frequency of 500 Hz for the event and the reference. Adding noise significantly increases the amplitude at higher frequencies. The noise overcomes the signal at higher frequencies which reduces the gradient of the log-spectral-amplitude-ratios. Δt^* was measured using 500 synthetic spectra with SNR from 1–7 for frequencies between 200–400 Hz (Figure 8c). This was done using the same reference event. Figure 8c shows that adding noise to the spectra causes an underestimate of Δt^* and that higher SNR leads to smaller errors. We calculate that events with a SNR >2 should be used. There is a tradeoff between the number of events to be used and reducing the error of the measurements. Although not shown, the method is less sensitive to the SNR of the reference event.

CHANGES IN ANISOTROPIC ATTENUATION WITH TIME

We select events from the cluster highlighted by Wuestefeld et al. (2011). This cluster contains 42 events, located in the spur of lots of events located to the east of the injection well. The log-spectral-amplitude-ratio method is applied to the two S-wave components polarised parallel ($S_{\parallel}$), and perpendicular ($S_{\perp}$) to the fracture strike. For completeness we also use the P-wave arrival, either the rotated component, or a stack of all three components, as performed by Kelly et al. (2013). First we use every event as a reference. Then the $S_{\parallel}$ is used as the reference event and compared to the $S_{\perp}$.

An increase in Δt^* of $S_{\perp}$ is observed during the half hour period of injection (Figure 9). $S_{\parallel}$ shows a decrease in Δt^* with time . We use Pearson's product-moment correlation coefficient, p, to describe the how positive or negative trend is. $S_{\perp}$ has a moderate positive correlation with time ($p = 0.44$). $S_{\parallel}$ has a moderate negative correlation with time ($p = -0.32$.) These trends are independent of the reference event chosen. Varying the frequency range (20–200 Hz, 100–300 Hz, or 300–500 Hz) or selecting different events, shows no systematic variation in Δt^* with time. P-wave attenuation for the rotated component does not demonstrate a correlation with time ($p = -0.08$). P-wave attenuation for the stacked component shows a moderate negative correlation ($p = -0.32$) with time(Figure 10).

Δt^* is a combination of changes in attenuation and travel time between the two events. The source location changes by up to 40 m within the cluster, thereby causing changes in travel time. Temporal changes in S-wave splitting also result in a change in travel times of S-waves, when a reduction in velocity means that the wave takes longer to reach the receiver. Wuestefeld et al. (2011) found a change in S-wave travel times of 2×10^{-3} s during this period. Using an estimate of Q = 50, as determined by Rutledge et al. (2004), and the

delay times measured by Wuestefeld et al. (2011), we theoretically predict the effect on Δt^* (Figure 9) to be 1×10^{-4} s. This is an order of magnitude smaller than that measured.

Comparing the two S-wave components by taking the log-spectral-amplitude-ratio (using $S_{\parallel}$ as a reference event)

INVERSION FOR FRACTURE PROPERTIES

To attempt to explain these measurements we used a simple inversion of the attenuation measurements to fit the model of Chapman (2003). We kept all the parameters the same as for the forward modelling (Table 1) except the fracture density which varied between 0–0.1. We then calculated a Δt^* from the model and matched it to the measurements.

This approach converts Δt^* measurements of the $S_{\perp}$ component into fracture density (Figure 12). This shows that the fracture density increased from 0.03 up to 0.07. This is much larger than the inferred fracture density estimated by Wuestefeld et al. (2011) from S-wave splitting (0.024–0.036), but there is more scatter in the fracture density derived estimate. It has strong positive correlation with time ($p = 0.61$).

Other parameters may affect the model, such as fluid, rock or fracture properties mentioned earlier. Aspect ratio is important in quantifying fluid flow through a fracture network. Assuming the fracture density calculated from S-wave splitting by Wuestefeld et al. (2011) is representative, we then search for changes to the aspect ratio of the fractures. We find that in order to match the measurements of delta t*, would require a decrease in aspect ratio over time, from 0.045 at the start to 0.005 at the end of the time period (Figure 13). Aspect ratio has moderate negative correlation with time ($p = -0.43$). In practice, hydraulic fracture stimulation could increase the fracture density and decrease the

aspect ratio, generating longer better connected fractures.

DISCUSSION

It is important to address the limitations of these measurements. Changes in travel time, frequency range, source parameters, and ray paths may all affect measurements of Δt^*. We also address the differences between fracture density derived from attenuation anisotropy and S-wave splitting measurements.

As stated previously, changes in travel time, be it from velocity changes or path length, will contribute to changes in Δt^*. However, the comparison between Δt^* values and those determined from travel time changes (Figure 9) show this to have a negligible effect in this case.

The frequency range used to calculate log-spectral-amplitude-ratios could also affect the results. Here fitting spectra between 200–400 Hz showed the clearest signal. This suggests that attenuation may only be independent of frequency over this limited range for this setting. There is also possible contamination from other phases, such as the P-wave coda, that may be interfering with this; further work is needed to investigate whether this is the cause.

Results reported are from one station, directly above the event locations and use events from a time where Wuestefeld et al. (2011) show a clear increase in fracture density. Other event-station pairs were also tested but no discernible trend could be found. The modelling shows that rays travelling close to vertical with a strike close to perpendicular to the fracture strike will show the most attenuation (Figure 3). This suggests that these event-station pairs show a temporal variation because of a preferential ray path to sample the

fractures. The other array, with 16 stations, may not be sampling a preferential azimuth for the fractures.

Changes in the spectral content of the sources for these events could also lead to changes in Δt^* measurements. However the waveforms are very similar for these events. The median normalised maximum correlation coefficient for all the events is 0.7 (Figure 14). This level of similarity suggests that these events likely form a repeating cluster as described by Rutledge et al. (2004). The magnitudes vary between -2.1 and -1.5, and show no systematic variation with time that could be causing the temporal variation in Δt^*.

We focus our interpretation on the S-wave polarised perpendicular to the fractures. The changes in P-wave attenuation for the rotated P-component are very small with a small correlation coefficient. The stacked P-wave changes are consistently negative for the stacked P-wave which is surprising and requires more work to understand. Significant changes in fluid properties, for example changing from hydrocarbons to the injected fracture fluid, could cause differences in attenuation between P-waves and S-waves. Changes to stress during the injection could also play a role. Our measurements show a slight decrease in Δt^* for S-waves polarised parallel to the fractures; which is difficult to explain. The model we use assumes perfectly aligned fractures which is unrealistic but a necessary simplification. It therefore cannot explain changes in the S-wave polarised parallel to the fracture strike.

Pearson's correlation coefficient is a measure of the linear dependence between two variables. In our case we can consider the dependence of the attenuation measurement with time. A coefficient of 1 would imply a perfect positive linear correlation, -1 a perfect negative linear correlation and 0 is no linear correlation. There is lots of scatter in our measurements and there is no reason to believe that fracture growth will lead to a linear correlation with

attenuation (see Figure 5). We therefore simply use the coefficient to determine if there is a statistically significant increase or decrease in attenuation with time.

The S-wave splitting measurements and the attenuation measurements give different fracture densities. The attenuation measurements suggest a greater amount of fracturing. The fracture density derived from S-wave splitting uses all available events and receivers for this time period whereas the measurements made here use a single receiver. This difference in sampling may explain the differences observed between datasets. The model used in Wuestefeld et al. (2011) does not take into account squirt flow and so is not sensitive to fluid parameters, permeability or the shape of the fractures. Therefore Wuestefeld et al. (2011) may be underestimating the amount of fractures by ignoring these effects. Our work here has examined this by assuming the fracture density derived from S-wave splitting measurements is correct and shown that a drop in fracture aspect ratio could cause these measurements of Δt^*. The fracture set is also unlikely to be perfectly aligned which both models assume. Therefore attenuation may be sensitive to more of the unaligned fractures than S-wave splitting. Further work is required to fully understand the differences because the possibility of measuring fracture and fluid parameters during hydraulic stimulation would lead to improvements in efficiencies and understanding of the mechanisms involved.

Our estimates suggest a change in fracture density of ~ 0.04. The fracture density ϵ_f is related to the void fraction, ϕ_f, (porosity) due to the fractures by: $\epsilon_f = \frac{3\phi_f}{4\pi r}$, where r is the aspect ratio of the fractures in Chapman (2003). Given this change in fracture density we can the calculate a change in porosity of 2×10^{-2} %. If we fill this porosity with the amount of fluid injected $\sim 400\,\mathrm{m}^3$ (40 bpm for 60 min) we can predict a minimum stimulated reservoir volume of $18 \times 10^5\,\mathrm{m}^3$. This would be represented by a sphere with a radius of 160 m. This assumes identical perfectly aligned fractures and that all the fluid injected goes

into these fractures. This volume is of a similar order to the cloud of injection, showing that this change in fracture density is realistic.

The results presented here show a temporal change in attenuation (Figure 9 and Figure 11). During this time period fluid is being injected at high pressure, and therefore it is highly likely that these attenuation changes are due to changes in the rock, fractures and their fluid content caused by the hydraulic stimulation process.

CONCLUSION

Anisotropic attenuation measurements are presented using passive seismic data from a hydraulic fracture stimulation treatment to investigate a new method to analyse the success of the stimulation. Δt^* is measured from a cluster of events from a half hour period within which fluid is injected. During this time period Δt^* had a correlation coefficient of 0.42 with time for S-wave polarised perpendicular to the inferred fracture strike. In contrast, S-wave polarised parallel to the fractures showed a negative correlation of -0.32. We also measured Δt^* between the parallel and perpendicular S-wave for each event and found a weak positive correlation with time of 0.22. We note that there is considerable scatter in the data, but the trends are robust and not dependent on the choice of reference event. The P-wave attenuation showed a small negative correlation with time (-0.08 for all the components stacked together and -0.32 for the rotated P component). Factors such as changes in source frequency, event location or S-wave splitting have been eliminated as potential causes and this temporal variation is attributed to changes in the medium. A squirt flow mechanism is the most likely explanation for this changing attenuation, and that this effect is dominated by the amount of fracturing. The Δt^* measurements can be interpreted as an increase in fracture density of 0.04. This is slightly larger than the increase in fracture

density as estimated from S-wave splitting data (Wuestefeld et al. (2011)), however both results show the same positive trend over the same time period and on a similar scale. This method provides a new tool for passive seismic monitoring of fracture network stimulation and fluid infiltration.

Future work should concentrate on expanding this technique to more datasets where a greater recording bandwidth may help the method. The method assumes a rock physics model with many poorly constrained parameters. A better understanding of these parameters and their variability would help to better interpret our observations. Ultimately a joint inversion of attenuation anisotropy and velocity anisotropy measurements may better constrain the problem.

ACKNOWLEDGEMENTS

The authors would like to thank: James Rutledge for providing the Cotton Valley dataset, members of the Bristol University Microseismicity Projects (BUMPS) consortium for helpful discussions on this work, and the reviewers and the associate editor for their contributions and guidance. Funding for this work has been provided by the sponsors of the BUMPS consortium and the NERC grant NE/L008351/1.

REFERENCES

Aki, K., and P. G. Richards, 2002, Quantitative seismology: University Science Books.

Al-Harrasi, O. H., 2010, Fractured reservoir characterisation using shear-wave splitting in microseismic data: A case study from Oman: PhD thesis, University of Bristol.

Al-Harrasi, O. H., J. M. Kendall, and M. Chapman, 2011, Fracture characterization using frequency-dependent shear wave anisotropy analysis of microseismic data: Geophysical Journal International, **185**, 1059–1070.

Baird, A., J. M. Kendall, and D. A. Angus, 2013a, Frequency-dependent seismic anisotropy due to fractures: Fluid flow versus scattering: Geophysics, **78**, WA111–WA122.

Baird, A., J.-M. Kendall, J. P. Verdon, A. Wuestefeld, T. E. Noble, Y. Li, M. Dutko, and Q. J. Fisher, 2013b, Monitoring increases in fracture connectivity during hydraulic stimulations from temporal variations in shear wave splitting polarization: Geophysical Journal International, **195**, 1120–1131.

Båth, M., 1974, Spectral Analysis in Geophysics: Elsevier Scientific Publishing Company.

Batzle, M. L., and Z. Wang, 1992, Seismic properties of pore fluids: Geophysics, **57**, 1396–1408.

Carter, A. J., and J. M. Kendall, 2006, Attenuation anisotropy and the relative frequency content of split shear waves: Geophysical Journal International, **165**, 865–874.

Chapman, M., 2003, Frequency-dependent anisotropy due to meso-scale fractures in the presence of equant porosity: Geophysical Prospecting, **51**, 369–379.

Chapman, M., S. Maultzsch, and E. Liu, 2003, Some Estimates of the Squirt-flow Frequency.: 2003 SEG Annual Meeting, 1–4.

Chichinina, T., V. Sabinin, and G. Ronquillo-Jarillo, 2006, QVOA analysis: P-wave attenuation anisotropy for fracture characterization: Geophysics, **71**, C37.

Clark, R. A., A. J. Carter, P. C. Nevill, and P. Benson, 2001, Attenuation measurements from surface seismic data: azimuthal variation and time-lapse case studies: 63rd EAGE metting, Amsterdam, The Netherlands, Expanded Abstarct, Session: L–28.

Dasgupta, R., and R. A. Clark, 1998, Estimation of Q from surface seismic reflection data: Geophysics, **63**, 2120–2128.

Eisner, L., D. Gei, M. Hallo, I. Opršal, and M. Y. Ali, 2013, The peak frequency of direct waves for microseismic events: Geophysics, **78**, A45–A49.

Johnson, J. H., M. K. Savage, and J. Townend, 2011, Distinguishing between stress-induced and structural anisotropy at Mount Ruapehu volcano, New Zealand: Journal of Geophysical Research, **116**, B12303.

Kelly, C. M., A. Rietbrock, D. R. Faulkner, and R. M. Nadeau, 2013, Temporal changes in attenuation associated with the 2004 M6.0 Parkfield earthquake: Journal of Geophysical Research: Solid Earth, **118**, 630–645.

Maultzsch, S., M. Chapman, E. Liu, and X.-Y. Li, 2007, Modelling and analysis of attenuation anisotropy in multiazimuth VSP data from the Clair field: Geophysical Prospecting, **55**, 627–642.

Maxwell, S., 2010, Microseismic: Growth born from success: The Leading Edge, **29**, 338–343.

Rutledge, J. T., W. S. Phillips, and M. J. Mayerhofer, 2004, Faulting induced by forced fluid injection and fluid flow forced by faulting: An interpretation of hydraulic-fracture microseismicity, Carthage Cotton Valley Gas Field, Texas: Bulletin of the Seismological Society of America, **94**, 1817–1830.

Shen, F., J. Sierra, D. Burns, and M. N. Toksöz, 2002, Azimuthal offset-dependent attributes applied to fracture detection in a carbonate reservoir: Geophysics, **67**, 355–364.

Teanby, N. A., J. M. Kendall, and M. van der Baan, 2004, Automation of shear-wave splitting measurements using cluster analysis: Bulletin of the Seismological Society of America, **94**, 453–463.

Titzschkau, T., M. Savage, and T. Hurst, 2010, Changes in attenuation related to eruptions of Mt. Ruapehu Volcano, New Zealand: Journal of Volcanology and Geothermal Research, **190**, 168–178.

Toksöz, M. N., and D. H. Johnston, 1981, Seismic Wave Attenuation: Society of Exploration Geophysicists.

Toksöz, M. N., D. H. Johnston, and A. Timur, 1979, Attenuation of seismic waves in dry and saturated rocks: I. Laboratory measurements: Geophysics, **44**, 681–690.

Verdon, J. P., J. M. Kendall, and A. Wuestefeld, 2009, Imaging fractures and sedimentary fabrics using shear wave splitting measurements made on passive seismic data: Geophysical Journal International, **179**, 1245–1254.

Verdon, J. P., and A. Wüstefeld, 2013, Measurement of the normal/tangential fracture compliance ratio (ZN/ZT) during hydraulic fracture stimulation using S-wave splitting data: Geophysical Prospecting, **61**, 461–475.

Walker, R. N. J., 1997, Cotton Valley hydraulic fracture imaging project: SPE Annual Technical Conference and Exhibition.

Wuestefeld, A., J. P. Verdon, J. M. Kendall, J. Rutledge, H. Clarke, and J. Wookey, 2011, Inferring rock fracture evolution during reservoir stimulation from seismic anisotropy: Geophysics, **76**, WC157.

LIST OF TABLES

LIST OF FIGURES

(c), and fracture radius (d) cause changes an order of magnitude smaller, a change of up to 2.5×10^{-3} s. The red line indicates the default values used in the modelling. Note the different scale for t^* in (a) compared to (b), (c), and (d). The default values from Table 1 are used for the other parameters.

6 Changes in t^* at different frequencies for different fracture densities (labelled on each line). The log-spectral-amplitude-ratio method assumes frequency independent attenuation. Based on tests with real data a frequency of 200–400 Hz is used to calculate LSAR. For fracture densities around 0.02–0.03, predicted by Wuestefeld et al. (2011), this frequency range shows negligible changes in attenuation (highlighted in red). The default values from Table 1 are used for the other parameters.

7 An example of the log-spectral-amplitude-ratio method. The three components, P and two S-waves ($S_{\parallel}$ and $S_{\perp}$), of the windowed seismogram for the event and the reference are shown (a) and (b). (c) The Fourier transform of the wavelets and a pre-event noise window are shown for the $S_{\perp}$. (d) The log-spectral-amplitude-ratio between the two events is calculated and a line is fit between the bandwidth of 200–400 Hz. The gradient of the line is proportional to Δt^*. (e) shows the spectrum of and $S_{\perp}$ and their appropriate noise windows. (f) shows the log-spectral-amplitude-ratio between the two phases of the same event following the method of Carter and Kendall (2006).

8 (a) Log-spectral-amplitude-ratios using a reference event with corner frequency of 300 Hz and corner frequencies of 50–500 Hz for the other events. (b) Log-spectral-amplitude-ratios estimated for events with varying signal to noise ratios (SNR). Gaussian noise was added to synthetic spectra; an increase in noise leads to a less stable log-spectral-amplitude-ratio. (c) Δt^* measurements from 500 synthetic spectra with SNR from 1–7 using a frequency range of 200–400 Hz. Note that the error in Δt^* is small for SNR > 2.

9 An example of the increase in Δt^* with time for the $S_\perp$ phase with changes in the $S_\parallel$ phase. The same reference event at 09:30 is used for both $S_\perp$ and $S_\parallel$. Theoretical changes in Δt^* due to changes in travel time from changes in velocity and event location are plotted in green.

10 The measured change in attenuation, Δt^*, for P arrivals, both from the P component (red) and the stack of the three components (blue).

11 Changes in Δt^* with time, for the $S_\perp$ phase using the $S_\parallel$ phase as a reference phase in the LSAR.

12 The estimated change in fracture density from attenuation measurements (red) and the S-wave splitting analysis of Wuestefeld et al. (2011) (blue).

13 Inversion for aspect ratio (blue) assuming the fracture densities derived from S-wave splitting measurements in Wuestefeld et al. (2011) (green).

14 Δt^* is also affected by changes in the source. Rutledge et al. (2004) showed that sources within each cluster were similar. The similarity of the waveforms suggest these events form a repeating cluster with the same source mechanism. The median value of the maximum normalised cross correlation coefficients is 0.7.

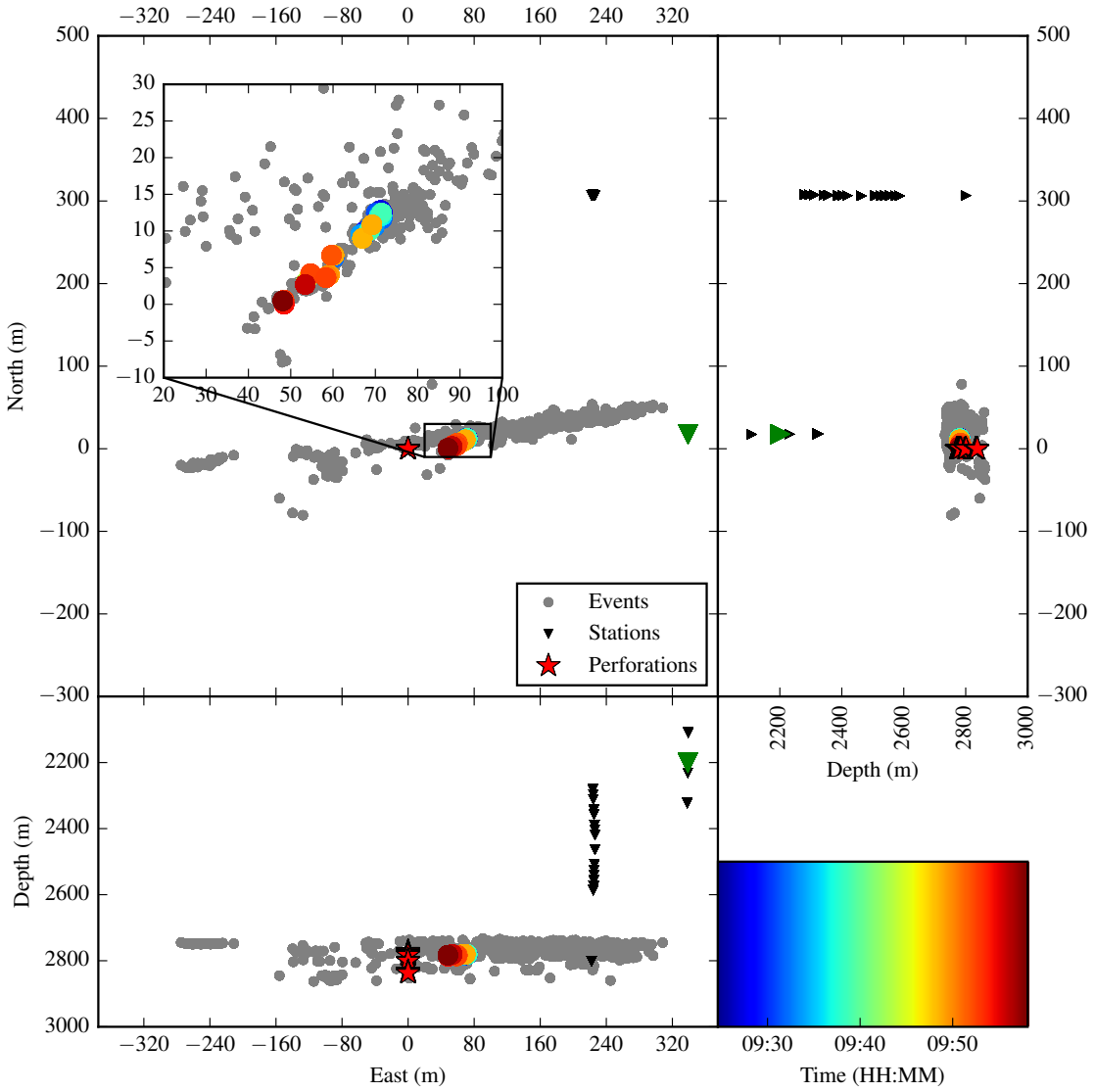

Figure 1: Location of events (circles), receivers (triangles) and injections (stars) from Rutledge et al. (2004). The receivers used in this study are shown in green. Events used in this study are coloured by the time at which they occurred, as indicated by the colour scale. The event cloud is well contained in depth and has a linear trend in map view. The events used in this study have been selected from a spur which contains over 42% of events located and has a slightly different trend to the rest of the event locations.

–

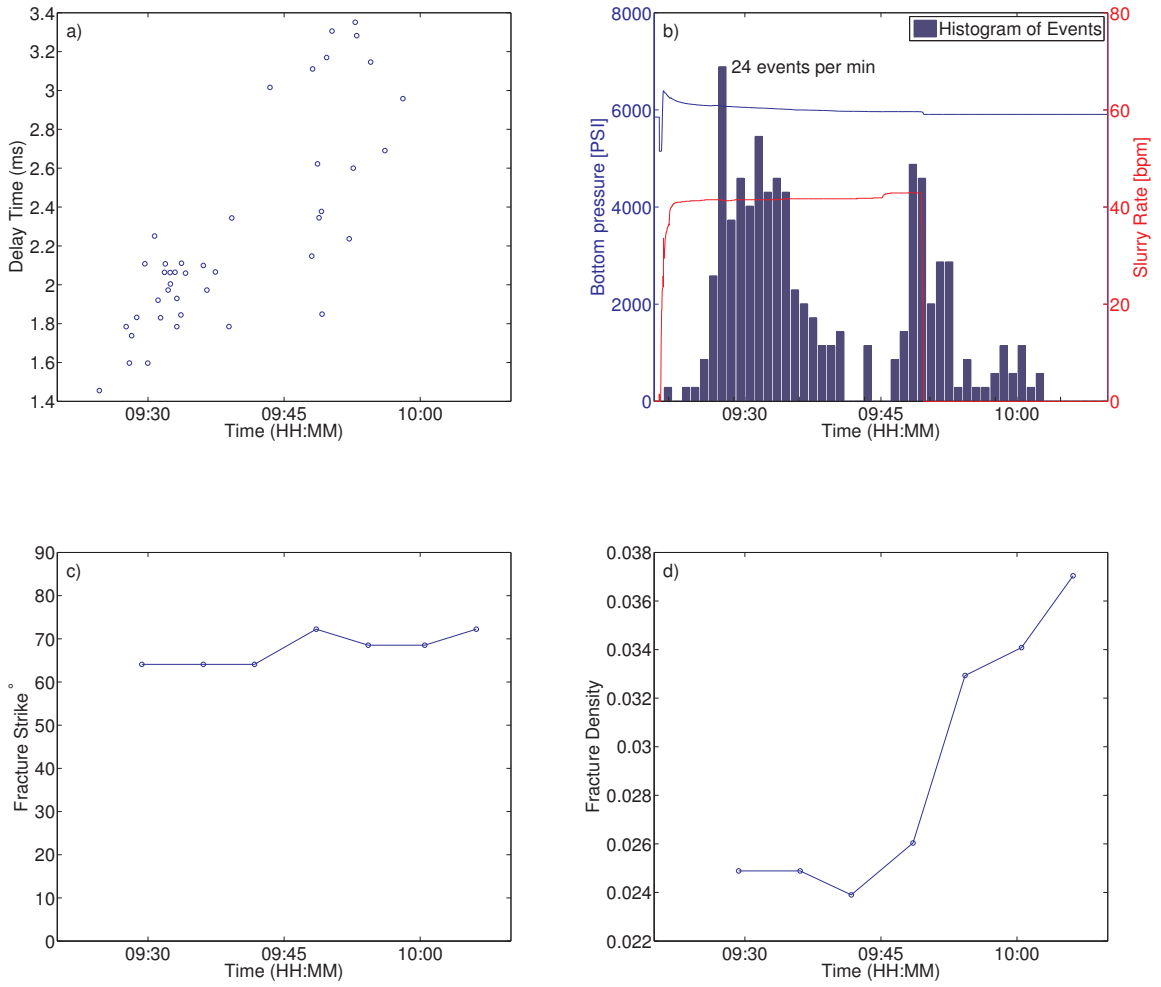

Figure 2: (a) Delay time from S-wave splitting measurements of a subset of events from Wuestefeld et al. (2011) as a function of time. (b) Histogram of the number of events along with bottom pressure and slurry rate of the injection. (c) Fracture strike and (d) fracture density derived from the inversion of splitting measurements using the technique of Verdon et al. (2009). Fracture density shows an increases over the time interval.

Property	Default Value	Range of Values	Source
Ray Azimuth (°)	92	0 - 360	From the Data
Ray Inclination (°)	25	0 - 360	From the Data
Frequency (Hz)	300	0 - 500	From the Data
Ray Distance (m)	645	0 - 1000	From the Data
P-wave Velocity (m/s)	5115	-	Rutledge et al. (2004)
S-wave Velocity (m/s)	2925	-	Rutledge et al. (2004)
Reference Frequency (Hz)	40	-	Estimated
Density (kg/m^3)	2542.7	-	Rutledge et al. (2004)
Porosity	0.1	0 - 0.2	Estimated
Permeability (milli darcy)	0.1	10^{-4} - 10^2	Estimated
Fracture Density	0.025	0 - 0.1	Wuestefeld et al. (2011)
Fracture Strike (°)	67	0-360	Wuestefeld et al. (2011)
Fracture Radius (m)	1.0	0-5	Estimated
Fracture Aspect Ratio	11×10^{-4}	0-0.06	Estimated
Fluid Viscosity (Poise)	1.5	0 - 2	Rutledge et al. (2004)
Fluid Bulk Modulus (Pascals)	1×10^8	10^6 - 10^{12}	Batzle and Wang (1992)

Table 1: The properties used in the modelling of attenuation. They have been either estimated, calculated from the data or an estimate is taken from previous work. The default ray properties are averaged values for the rays between the events and the receiver used in this study.

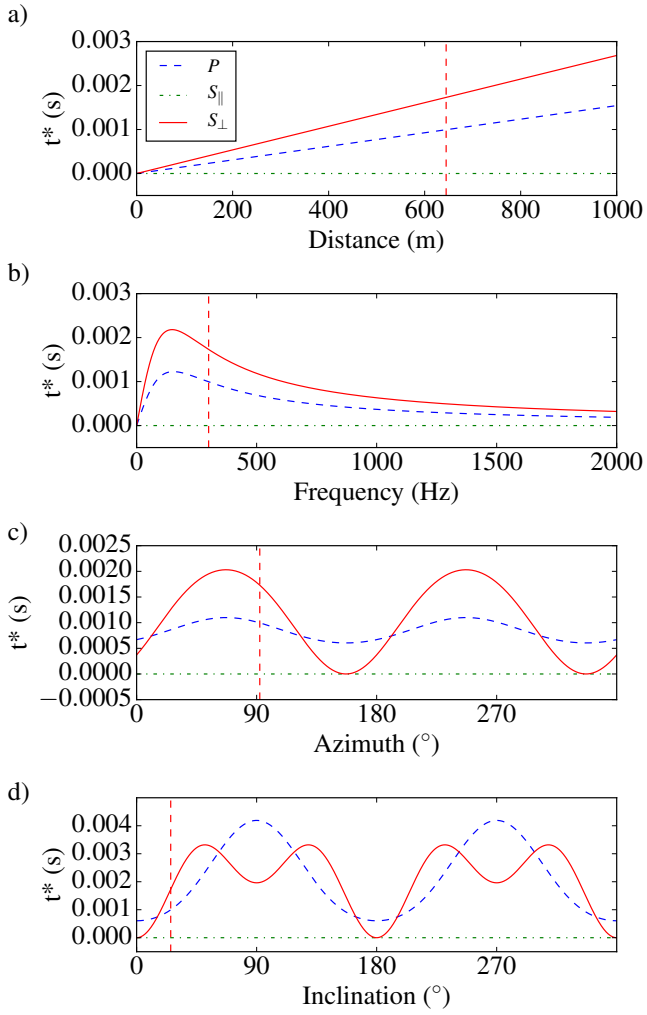

Figure 3: The effect of different ray properties on t^*. The ray properties are known from the data (the red dashed line) but any variation in these would cause variation in t^* which is proportional to attenuation. The default values from Table 1 are used for the other parameters.

–

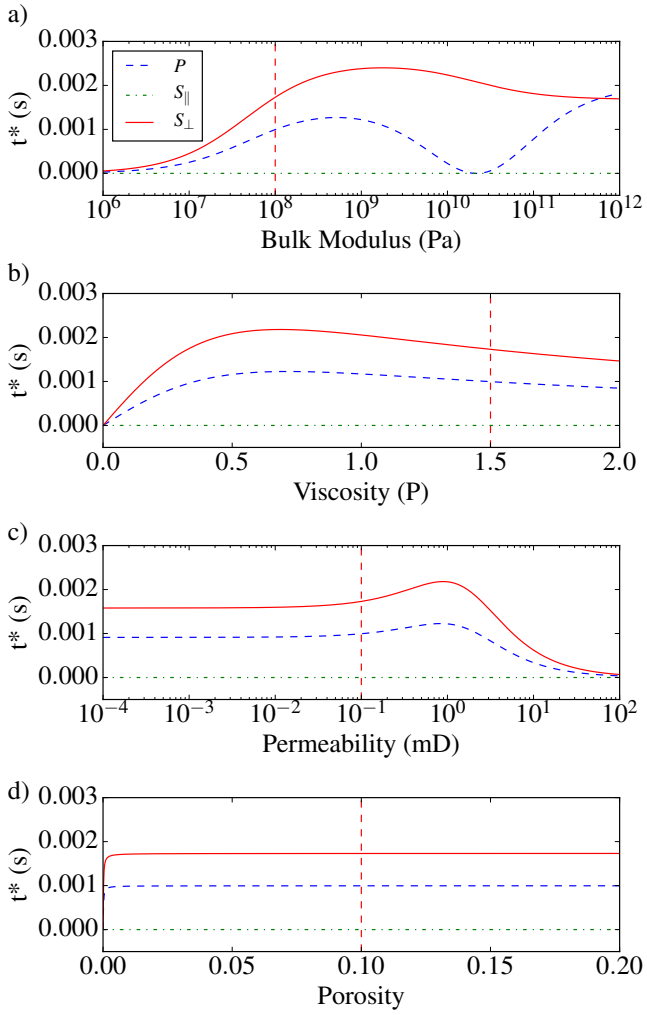

Figure 4: The effect of different rock and fluid properties on t^*. t^* which is proportional to attenuation does not vary significantly near the estimated values for the Cotton Valley formations, the red dashed lines, except for the bulk modulus but this is probably the best constrained parameter and is shown here varying over a logarithmic range of values. The default values from Table 1 are used for the other parameters.

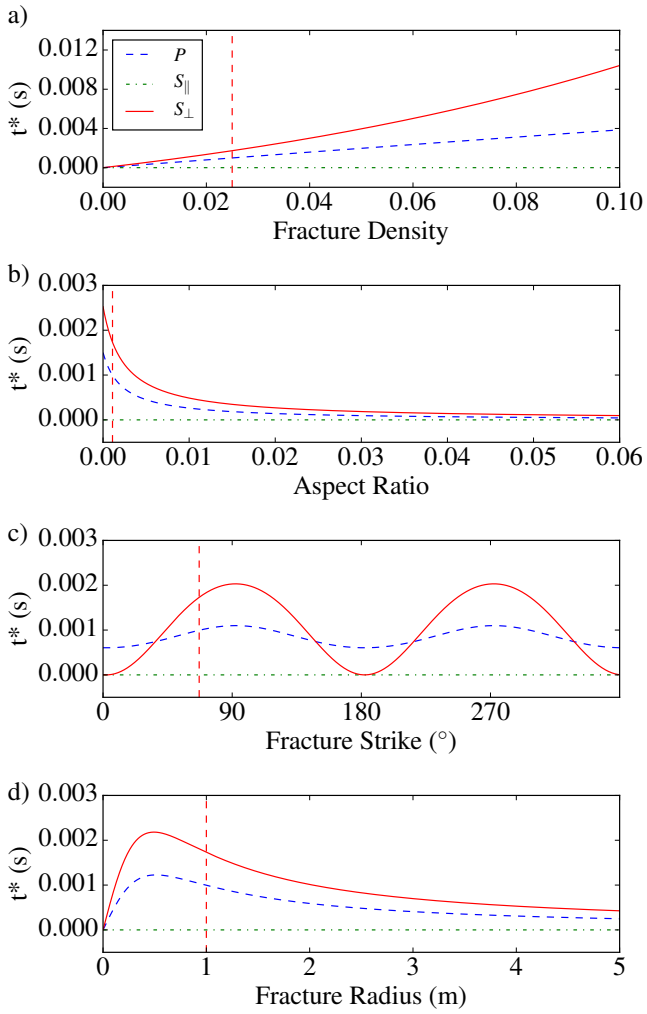

Figure 5: Changes in t^* due to changes in fracture properties according to the squirt flow model of Chapman (2003). Fracture density (a) causes the largest effect with a range of 0–0.012 s due to an increase in fracture density from 0–0.01. Aspect ratio (b), fracture strike (c), and fracture radius (d) cause changes an order of magnitude smaller, a change of up to 2.5×10^{-3} s. The red line indicates the default values used in the modelling. Note the different scale for t^* in (a) compared to (b), (c), and (d). The default values from Table 1 are used for the other parameters.

–

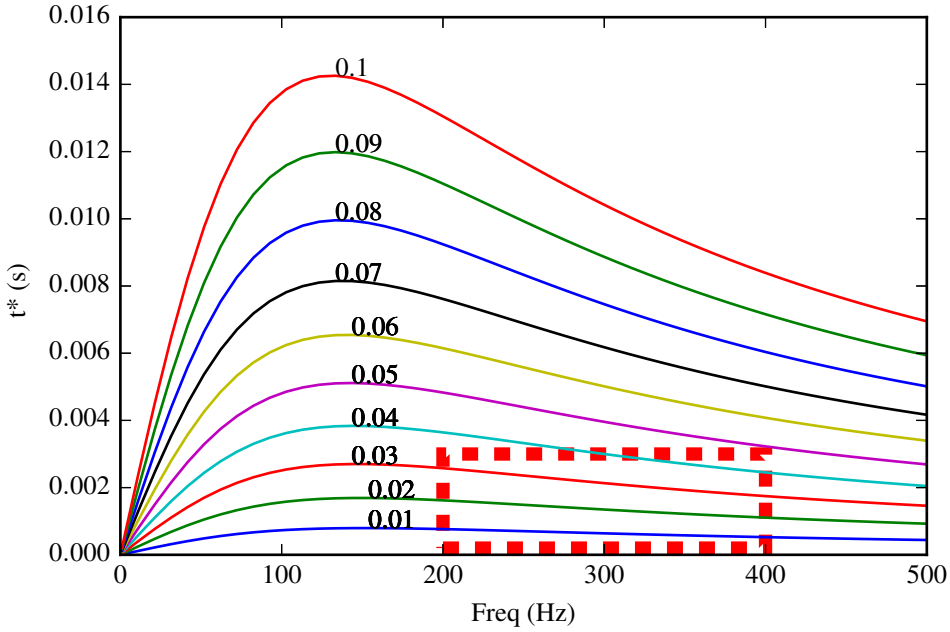

Figure 6: Changes in t^* at different frequencies for different fracture densities (labelled on each line). The log-spectral-amplitude-ratio method assumes frequency independent attenuation. Based on tests with real data a frequency of 200–400 Hz is used to calculate LSAR. For fracture densities around 0.02–0.03, predicted by Wuestefeld et al. (2011), this frequency range shows negligible changes in attenuation (highlighted in red). The default values from Table 1 are used for the other parameters.

–

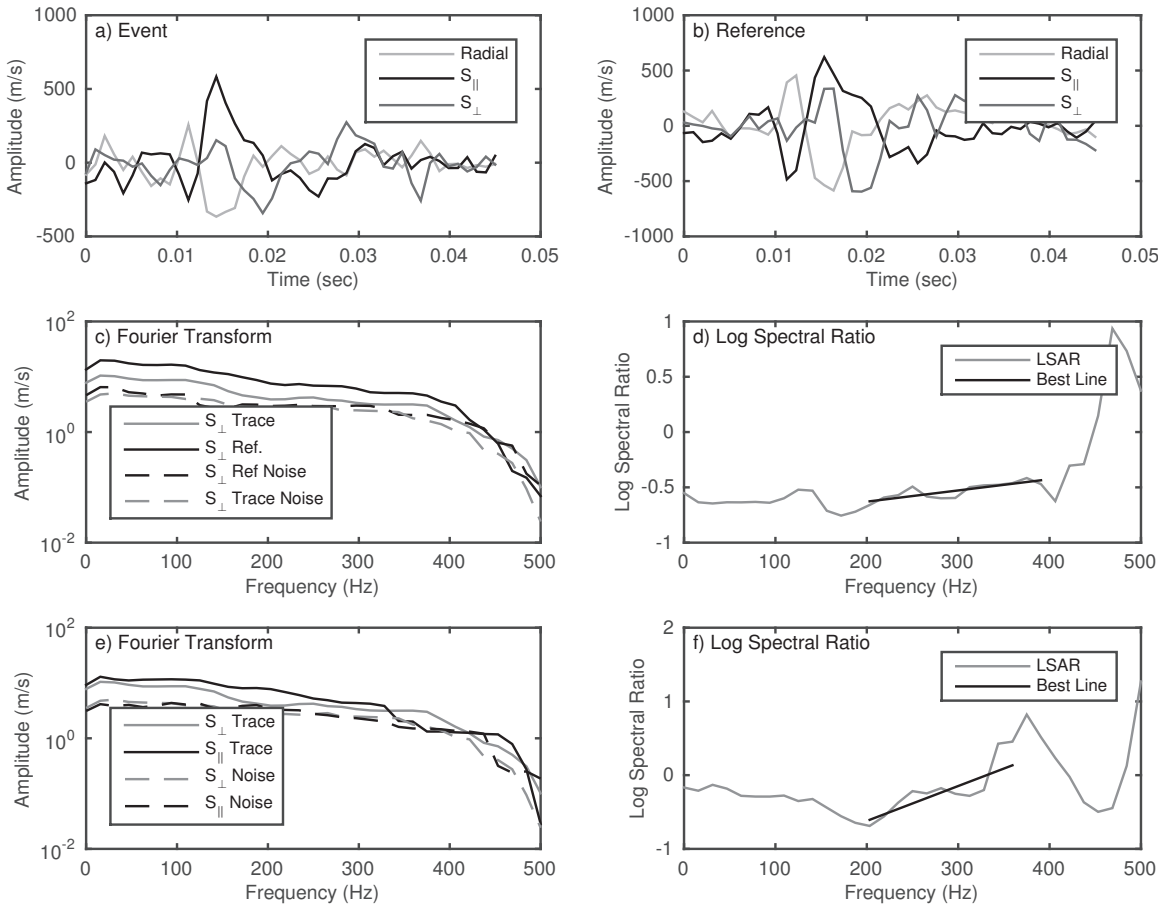

Figure 7: An example of the log-spectral-amplitude-ratio method. The three components, P and two S-waves ($S_{\parallel}$ and $S_{\perp}$), of the windowed seismogram for the event and the reference are shown (a) and (b). (c) The Fourier transform of the wavelets and a pre-event noise window are shown for the $S_{\perp}$. (d) The log-spectral-amplitude-ratio between the two events is calculated and a line is fit between the bandwidth of 200–400 Hz. The gradient of the line is proportional to Δt^*. (e) shows the spectrum of and $S_{\perp}$ and their appropriate noise windows. (f) shows the log-spectral-amplitude-ratio between the two phases of the same event following the method of Carter and Kendall (2006).

–

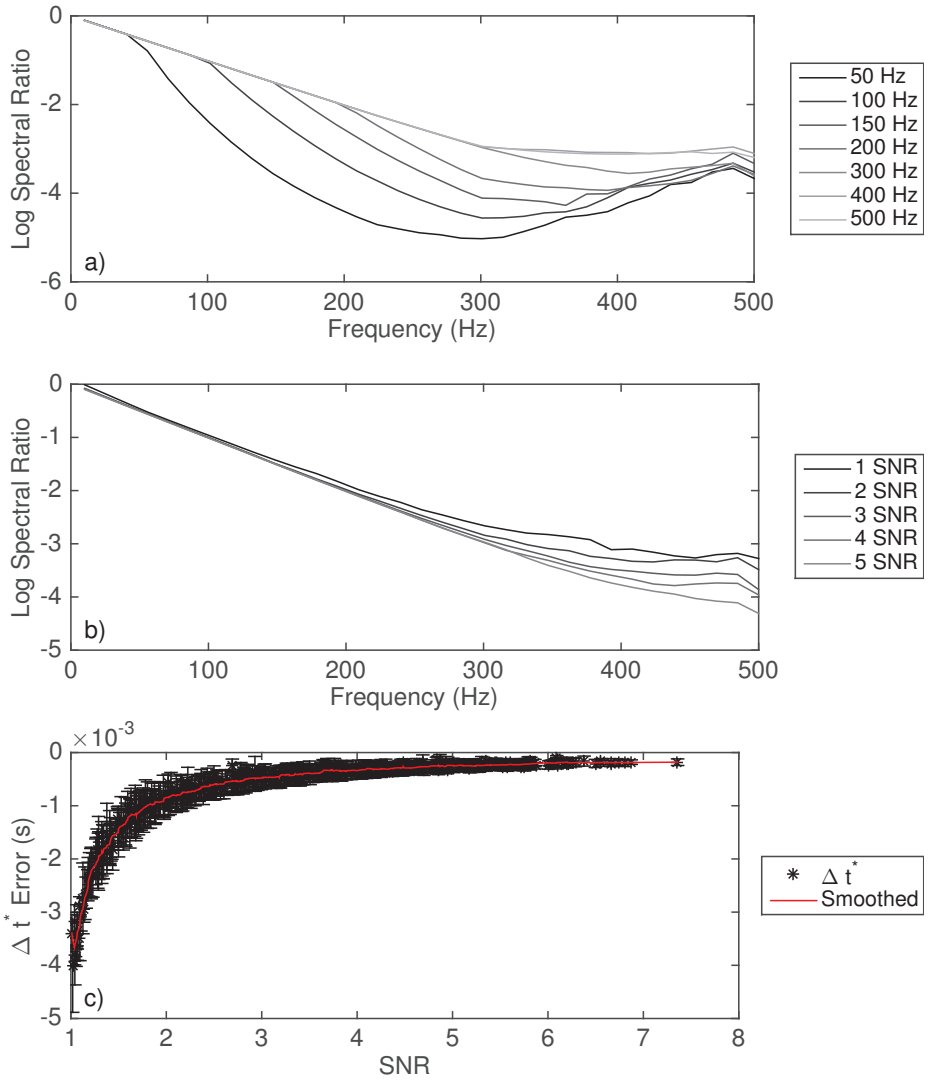

Figure 8: (a) Log-spectral-amplitude-ratios using a reference event with corner frequency of 300 Hz and corner frequencies of 50–500 Hz for the other events. (b) Log-spectral-amplitude-ratios estimated for events with varying signal to noise ratios (SNR). Gaussian noise was added to synthetic spectra; an increase in noise leads to a less stable log-spectral-amplitude-ratio. (c) Δt^* measurements from 500 synthetic spectra with SNR from 1–7 using a frequency range of 200–400 Hz. Note that the error in Δt^* is small for SNR > 2.

–

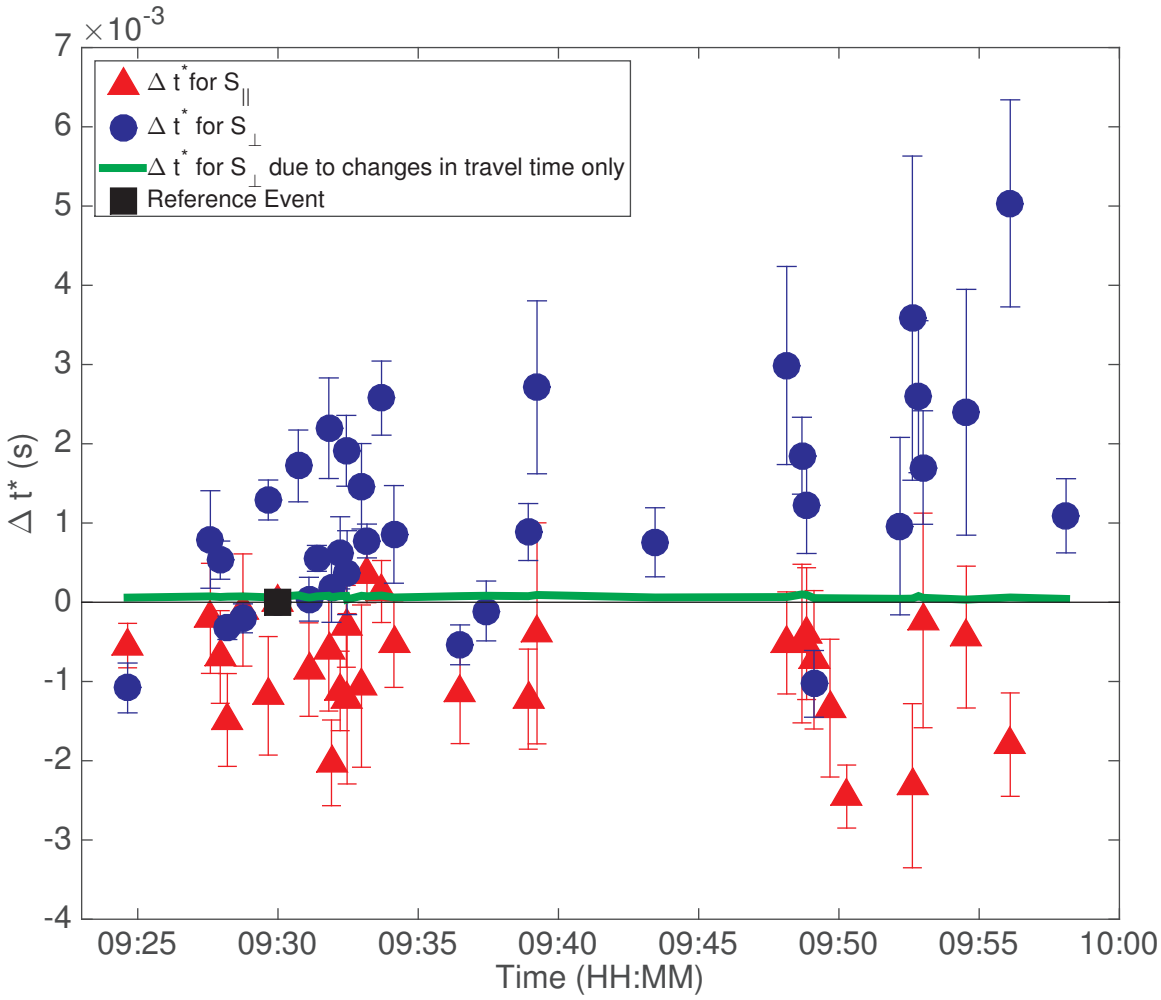

Figure 9: An example of the increase in Δt^* with time for the $S_\perp$ phase with changes in the $S_\parallel$ phase. The same reference event at 09:30 is used for both $S_\perp$ and $S_\parallel$. Theoretical changes in Δt^* due to changes in travel time from changes in velocity and event location are plotted in green.

–

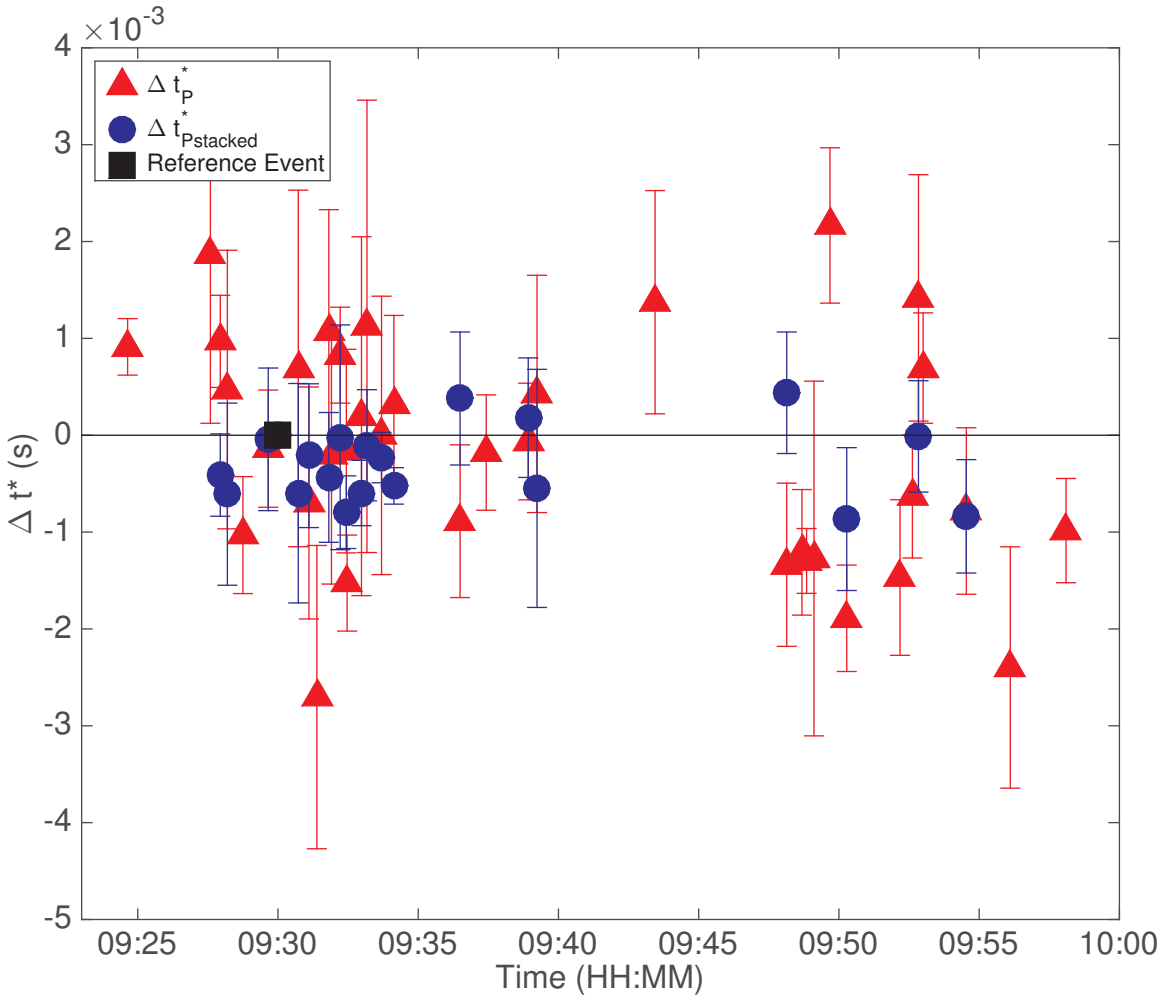

Figure 10: The measured change in attenuation, Δt^*, for P arrivals, both from the P component (red) and the stack of the three components (blue).

–

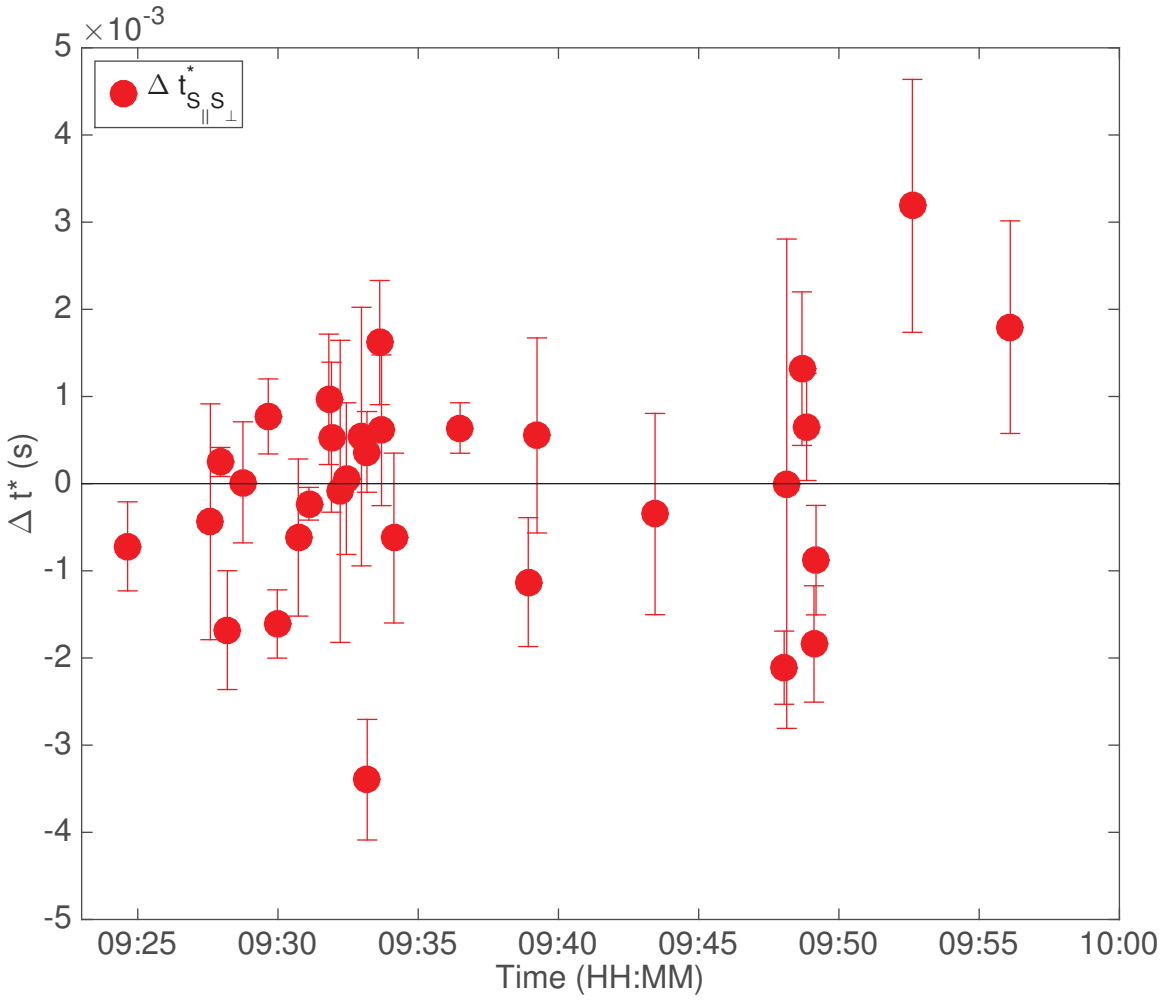

Figure 11: Changes in Δt^* with time, for the $S_\perp$ phase using the $S_\parallel$ phase as a reference phase in the LSAR.

–

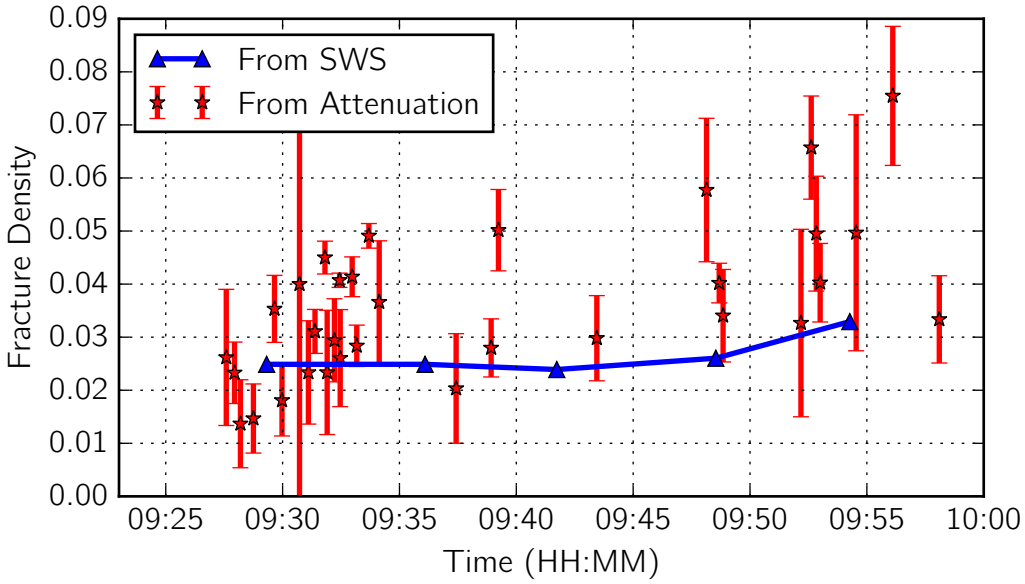

Figure 12: The estimated change in fracture density from attenuation measurements (red) and the S-wave splitting analysis of Wuestefeld et al. (2011) (blue).

–

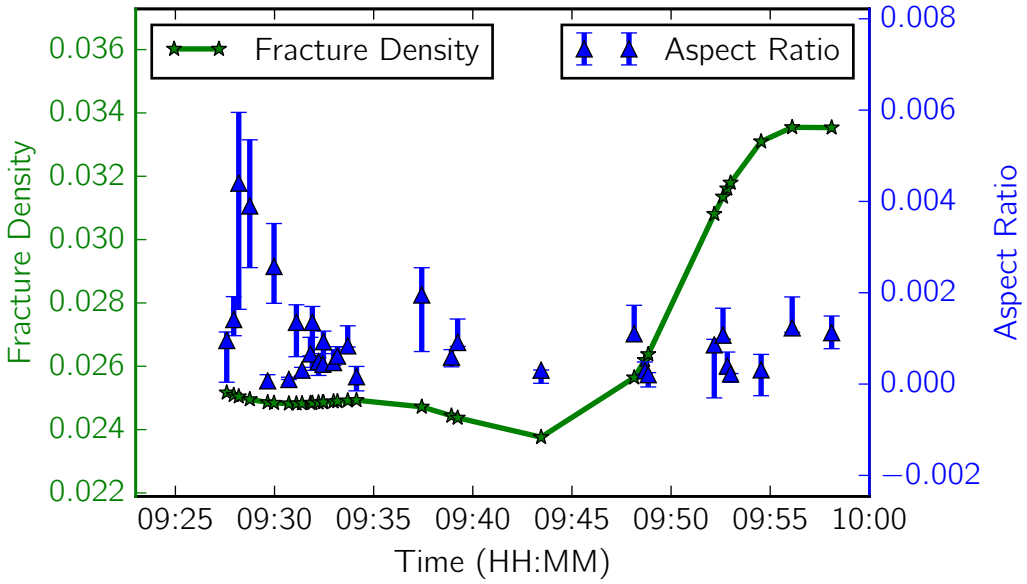

Figure 13: Inversion for aspect ratio (blue) assuming the fracture densities derived from S-wave splitting measurements in Wuestefeld et al. (2011) (green).

–

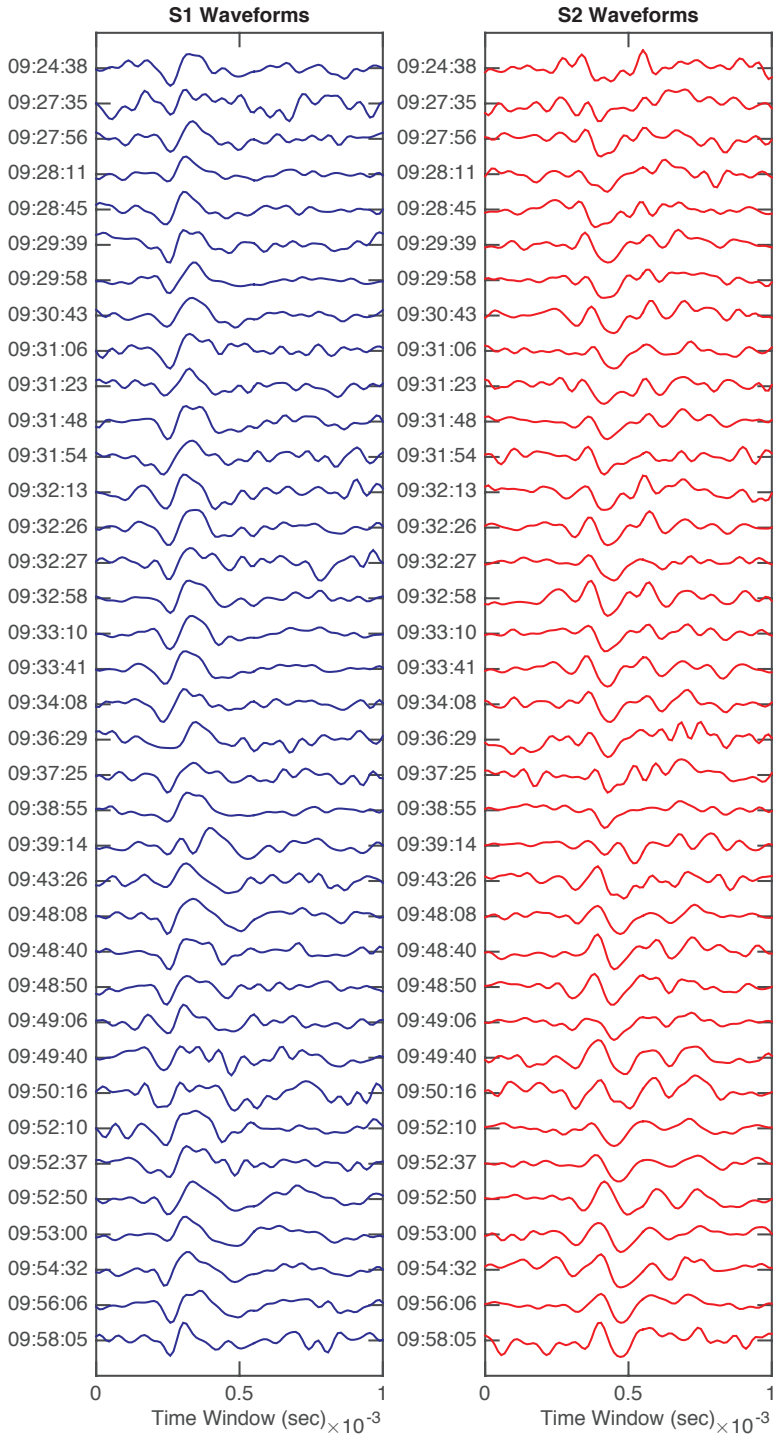

Figure 14: Δt^* is also affected by changes in the source. Rutledge et al. (2004) showed that sources within each cluster were similar. The similarity of the waveforms suggest these events form a repeating cluster with the same source mechanism. The median value of the maximum normalised cross correlation coefficients is 0.7.